Journal of Colloid and Interface Science 646 (2023) 606–615

Contents lists available at ScienceDirect

Journal of Colloid And Interface Science

journal homepage: www.elsevier.com/locate/jcis

Suppression of droplet pinch-off by early onset of interfacial instability

Rutvik Lathia, Chandantaru Dey Modak, Prosenjit Sen *

Centre for Nano Science and Engineering, Indian Institute of Science, Bangalore 560012, India

GRAPHICAL ABSTRACT

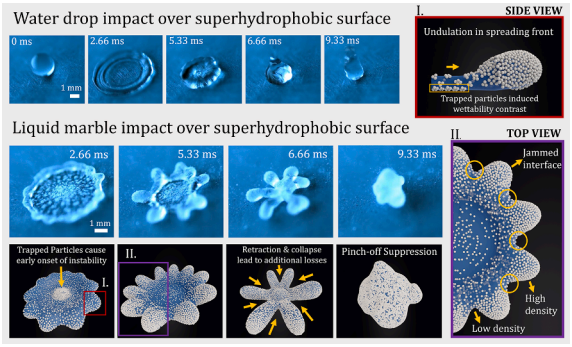

ARTICLE INFO

Keywords:
Droplet impact
Particle coating
Liquid Marble
Fingering instability
Droplet fragmentation

ABSTRACT

Hypothesis: Interfacial instabilities cause undesirable droplet breakage during impact. Such breakage affects many applications, such as printing, spraying, etc. Particle coating over a droplet can significantly change the impact process and stabilize it against breakage. This work investigates the impact dynamics of particle-coated droplets, which mostly remains unexplored.

Experiments: Particle-coated droplets of different mass loading were formed using volume addition. The prepared droplets were impacted on superhydrophobic surfaces, and their dynamics were recorded using a high-speed camera.

Findings: We report an intriguing phenomenon where an interfacial fingering instability helps suppress pinch-off in particle-coated droplets. This island of breakage suppression, where the droplet maintains its intactness upon impact, appears in a regime of Weber numbers where bare droplet breakage is inevitable. The onset of fingering instability in particle-coated droplets is observed at much lower impact energy, around two times less than the bare droplet. The instability is characterized and explained using the rim Bond number. The instability suppresses pinch-off because of the higher losses associated with the formation of stable fingers. Such instability can also be seen in dust/pollen-covered surfaces, making it useful in many applications related to cooling, self-cleaning, anti-icing etc.

* Corresponding author.
E-mail address: prosenjits@iisc.ac.in (P. Sen).

https://doi.org/10.1016/j.jcis.2023.05.067
Received 6 February 2023; Received in revised form 5 May 2023; Accepted 10 May 2023
Available online 16 May 2023

1. Introduction

Droplet breakage on impact is undesirable. It affects essential applications such as printing, spraying (e.g., pesticides), coating, bioreactors, cooling, and directional transport [1–3]. In printing, droplet breakage leads to the generation of undesired spots and compromises printing resolution. In the case of spraying on plants, ejected droplets are lost to the ground and cause environmental pollution [4]. Similar droplet breakage also causes pollution during fertilizer production [3]. Smaller droplets are more efficient in spreading viruses and diseases than larger ones. Thus, smaller droplet generation due to impact breakage enhances the spreading of pathogens and diseases in plants [5,6] and humans [7] onto a larger area.

Droplet impact on superhydrophobic surfaces is studied for its implications in various applications and natural phenomena. On impact, the droplet spreads, and its kinetic energy is stored as surface energy. It converts back into kinetic energy during rebound. While the top part of the droplet rapidly moves away from the surface, the bottom part leaves the surface slowly as adhesion delays detachment [8]. This process results in the stretching of the droplet with its stretched length (L_{max}) larger than the maximum spread diameter (D_{max}). Stretching increases with impact velocity. Beyond a critical Weber number, the stretching is sufficient to enable the ejection of smaller droplets from the top. Weber number is defined as $We = \rho V^2 D_0/\gamma$, where ρ, V, D_0 and γ are density, impact velocity, diameter, and surface tension, respectively. Such breakage is driven by Rayleigh-Plateau (RP) instability and occurs during the lift-off phase [9]. RP instability is commonly observed in falling streams of liquid where unstable perturbations with wavelengths larger than the circumference are responsible for the stream breaking into smaller droplets. Thus, the droplet pinch-off happens if the interface stretches beyond a critical value during the lift-off stage.

A further increase in impact velocity results in droplet dissociation on the impact surface itself. Such dissociations on the surface are of mainly two types: receding breakup and splashing [10,11]. Receding breakup happens during the retraction of the droplet from a surface after achieving maximum spread. Contrarily, the splashing happens during the spreading phase of the droplet and occurs at slightly higher impact velocities than receding breakup. Both of these dissociations are primarily caused by the instability that occurs at the spreading droplet front. Previous literature has suggested that the Rayleigh-Taylor (RT) and Rayleigh-Plateau (RP) instabilities play a combined role in such dissociations [12–14]. RT instability results from rapid deceleration of the droplet rim during the impact. Additionally, the toroidal rim is susceptible to RP instability. Instability-driven perturbations grow during the impact, resulting in droplet breakage on the surface.

Impact outcomes of bare droplets on various surfaces have been reported in many pieces of literature [2,15,16]. Mechanical properties of hydrophobic granular rafts under small interface deformations have been studied by Planchette et al. [17]. In this work, the impact of particle-coated droplets on superhydrophobic surfaces has been pursued. Particle-coated droplets are commonly known as liquid marbles (LM) [18]. There have been a few reports of LM impact on hydrophobic, hydrophilic surfaces [19,20] and other particle-armored interfaces [21]. These studies have mainly focused on investigating the spreading behavior of the LM. Also, liquid marble's impact over other liquid marble has been reported for applications related to droplet manipulations [22]. Recently, particle layer de-coating has been reported by impacting liquid marble on a soap film [23]. Moreover, the impact of liquid marbles over a particle bed can be utilized in the formation of Janus and small liquid marble [24,25].

Interestingly for LM, as the impact velocity increases, droplet breakage does not progress from pinch-off to a receding breakup regime. The pinch-off regime is shortened, and we observe complete suppression of droplet breakage in LM for a range of higher impact velocities (1.25 m/s to 1.62 m/s). This is attributed to a fingering instability in LM, which helps it stabilize against breakage. Such fingers are also present in the case of droplet impact over superhydrophobic surfaces but at much higher velocities (>1.76 m/s). There have been many studies on the instability aspect of bare droplet impacts [13,26–30], but none on liquid marble. Additionally, in the case of droplets, the stability of the finger is not present as it breaks into several droplets [13,26–30]. The reported inertial-capillary fingering instability in this paper differs from the commonly observed viscous fingering in the case of particle-laden interfaces [31].".

The fingering instability is also observed for bare droplet impact on particle laden surfaces. Such scenarios help in understanding the interactions of droplets with particles in self-cleaning applications and pollen dispersion [6,32–34]. This study will be helpful in applications such as in the production of mechanically stable bioreactors [35,36]. The present study helps us understand the dynamics of particle-coated curved interfaces at large deformations, which are largely unexplored. LM has also been used as a biological model [37]. Studying its large-deformation dynamics helps us understand the response of organs and cells under sudden impact conditions such as accidents [38]. As the applications of LM in the digital microfluidics platform are increasing [39], the present paper also helps design such applications better.

2. Materials and methods

2.1. Preparation of liquid marble

A polytetrafluoroethylene (PTFE) powder with an average particle diameter of 35 μm was used to prepare liquid marble (with a DI water core liquid of 8.2 μL) by the rolling method [40]. To estimate the particle wettability, the PTFE solution was coated on flat glass. The contact angle of water on PTFE was measured to be 119° (Supplementary Fig. S1(B)). Because of the higher contact angle, it is energetically unfavorable for the particle to go inside the drop; thus, it stays at the air–liquid interface only. Control of the mass loading (ML) was obtained by creating smaller liquid marble (LM) of different volumes with full surface coverage. Then the LM is placed on a superhydrophobic surface with a bare droplet. A superhydrophobic surface is required to avoid rupturing of LM with lower ML. Collision of the LM with a bare droplet result in merging and forming a larger LM, as shown in Fig. 1(A). The final LM volume was 8.2 μL. The geometric relation $S^3 \sim V^2$ determines the initial LM volume, where S and V are the surface area and the volume of the liquid drop, respectively [41]. The different volumes of LMs and water droplets used to prepare various ML are described in Table 1. Where V_{LM} and V_W represent the volume of liquid marble and the volume of water drops. The ML and density (ρ) were determined by averaging the mass of ten liquid marbles after completely drying the liquid.

2.2. Preparation of superhydrophobic surface

The superhydrophobic copper surface was prepared by the method reported previously [42,43]. A copper substrate (3 cm × 2 cm) was cleaned with acetone, isopropyl alcohol (IPA), and deionized (DI) water. This was followed by a 30 s cleaning with sulfuric acid (33% in DI water). The cleaned copper surface was then immersed in an aqueous solution of sodium hydroxide (2.5 mol/L) and ammonium persulfate (0.1 mol/L) for 20 min at room temperature. This solution etches the copper surface and produces copper hydroxide nanowires on the surface (Supplementary Fig. S1). The substrate is cleaned multiple times with DI water and dried with nitrogen. The substrate is dipped in Teflon solution for 10 min to get a superhydrophobic surface. Subsequently, it is dried by heating at 110 °C for 10 min. The prepared superhydrophobic surfaces show excellent repellency with a water contact angle of 171° (Supplementary Fig. S1).

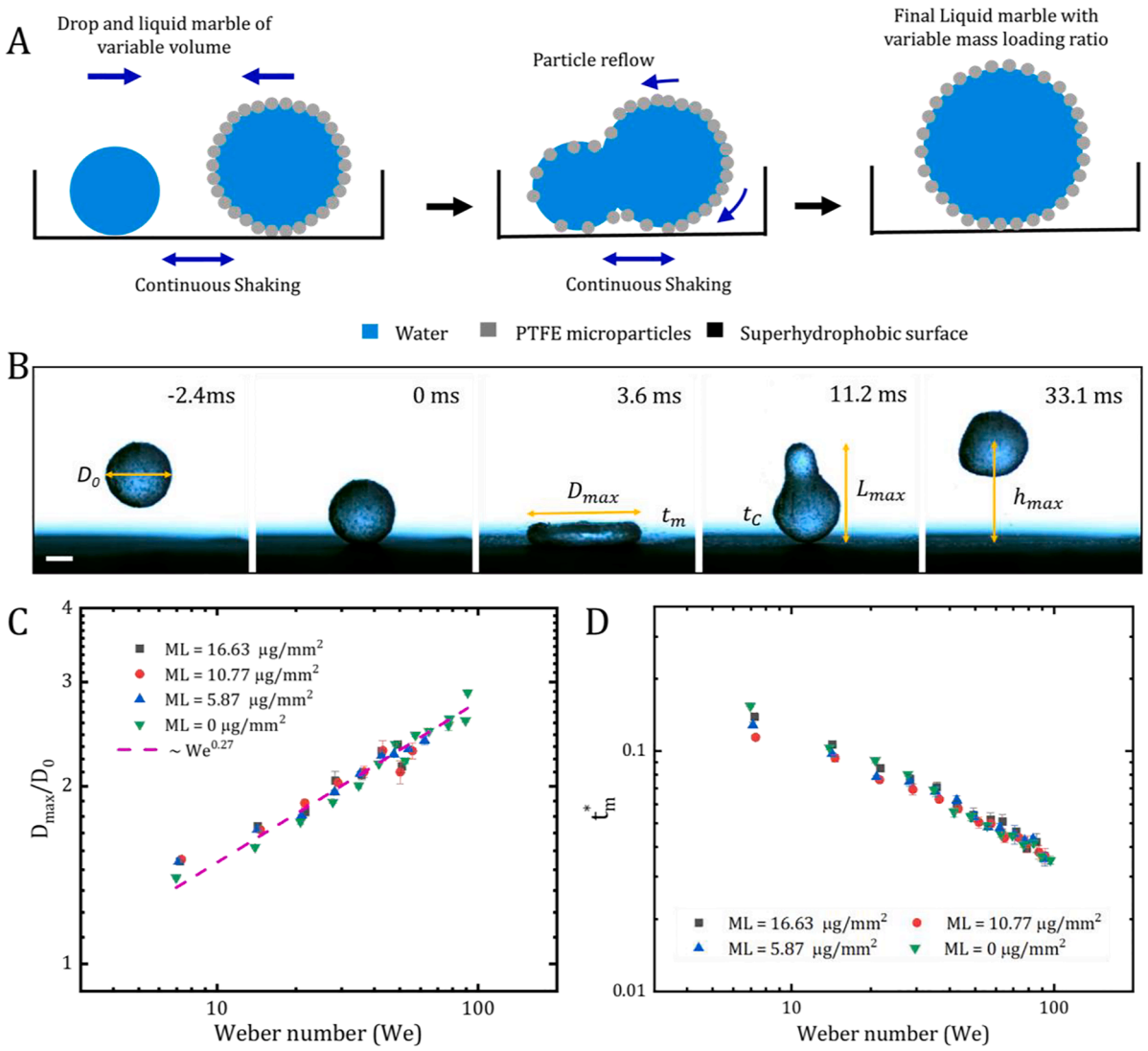

Fig. 1. (A) Methodology for the preparation of LM with variable ML. First, a smaller volume LM with maximum ML is prepared. The LM volume is increased by merging with a bare droplet. The droplet volume is taken such that the final volume of the LM will be 8.2 μL. Vibration is necessary to ensure uniform particle distribution across the surface. (B) Parameters measured during LM impact. Where D_0, D_{max}, t_m, t_c, $L_{max,}$ and $h_{max,}$ are the initial diameter of the LM, maximum spread diameter, maximum spreading time, contact time, maximum length during rebound, and the maximum height of rebound, respectively. (Scale bar – 1 mm). (C) The normalized maximum diameter plotted against *We*. Power law fit leads to $We^{0.27}$. (D) The maximum spread time (t_m) normalized with drop inertia-capillary time based on maximum spread diameter ($\tau \sim \sqrt{\rho D_{max}^3/\gamma}$).

Table 1
The values of volume to be taken for particular ML. As described in the main text, various sizes of LM and droplets collision results in different ML. V_{LM} and V_W represent the volume of liquid marble and water droplet, respectively. The final volume of LM used in our experiments is fixed at 8.2 μL.

V_{LM} (μL)	V_w (μL)	ML (μg/mm²)	$\rho(kg/m^3)$
0	8.2	0	997
1.58	6.62	5.87 ± 0.49	1004
4.46	3.74	10.77 ± 0.47	1011
8.2	0	16.63 ± 0.5	1017

2.3. Droplet impact experiments

Prepared LM with different mass loadings are impacted over a superhydrophobic surface. Impact velocity was controlled by impacting the LM from different heights with the help of 3D printed release mechanism which ensures no pre-velocity and rotation (Supplementary section 1.1 and Supplementary Fig. S1(A)). The dynamics were recorded with a high-speed camera. The recorded images were analyzed for measuring different parameters, as shown in Fig. 1(B).

3. Results and discussion

3.1. The dynamic surface tension of LM during impact

For static scenarios, LM has reduced effective surface tension. As shown in Supplementary Fig. S1(D), the effective surface tension (γ_{eff}) is determined by the maximum puddle height method [44]. The effective surface tension decreases with ML increase. For lower mass loaded LM, γ_{eff} stays near the bare droplet. Whereas, for higher mass loading γ_{eff} decreases significantly to ~ 50 mN/m. However, in the case of droplet impact, the dynamic surface tension of the LM determines the interface dynamics. The value of dynamic surface tension lies between the water surface tension and the effective surface tension (γ_{eff}) of LM. During spreading, the newly created surface is primarily a water surface with very few particles; thus, the change in net surface energy during the

spreading process is determined by the water surface tension. Thus, as an approximation, water surface tension (~72 mN/m) has been used as the dynamic surface tension in our case. This scenario is analogous to the impact of droplets with slow diffusing surfactants [45,46].

The spreading dynamics of an LM show approximately the same behavior and scaling as a bare droplet. Maximum spreading diameter (D_{max}) on the superhydrophobic surface is known to follow $D_{max} \sim D_0 \, We^{0.25}$ scaling [15]. LM follows approximately the same scaling $D_{max} \sim D_0 \, We^{0.27}$ (Fig. 1(C)). As shown in Fig. 1(D), the maximum spread time (t_m) normalized with the inertia-capillary time scale based on maximum spread ($\tau \sim \sqrt{\rho D_{max}^3/\gamma}$) is also similar. Since the maximum spreading diameter also remains the same for LM and bare droplet, the normalization of time based on original diameter ($\tau \sim \sqrt{\rho D_0^3/\gamma}$) also result in collapse (Supplementary Fig. S1(E)). Both these observations justify the use of water surface tension as an approximation for LM's dynamic surface tension.

3.2. Impact outcome

The rebound of the LM follows entirely different retraction dynamics, which leads to a different outcome for the impact process. With an increase in impact velocity for a bare droplet, the outcome progresses from a no-breakage to pinch-off to receding-breakup, as shown in Fig. 2. As the impact velocity increases, LM breakage does not progress from pinch-off to receding-breakup regime (Supplementary Video S1). The pinch-off regime is shortened, and we observe complete suppression of LM pinch-off for a range of higher impact velocities (1.25 m/s to 1.62 m/s). In this zone, LM shows intactness and mechanical stability even at high *We* (57 to 92). However, further increase in *We* results in receding breakup (Supplementary Video S2) and splashing (Supplementary Video S3). Fig. 2(D) reveals that droplets with high Weber number ($We > 90$) undergo receding breakup, which is often accompanied by pinch-off events, particularly for lower ML liquid marbles. In contrast, Fig. 2(C) demonstrates that during lower Weber number conditions, only pinch-off events during lift-off are observed.

Traditional studies have shown that the increase in viscosity of Newtonian droplets results in the delay of pinch-off and in suppression of bouncing [47]. For LM's, the maximum spreading time and diameter of LM remains the same as bare droplets, indicating that their effective viscosities are similar. Further, unlike our current observations, Newtonian droplets with enhanced viscosity will only show a transition from no-breakage to breakage. Hence, an increase in viscosity cannot explain pinch-off suppression. Previous studies have attributed the suppression of droplet breakage to the addition of various polymers, with arguments focusing on non-Newtonian elongation viscosity [48]. A subsequent study has downplayed the role of non-Newtonian elongation viscosity in bouncing suppression [49]. The same study has indicated the role of enhanced contact line dissipation in these polymer solutions. However, there is a marked distinction in the contact line retraction velocity for polymer solutions. As discussed later in the text, we do not observe any such difference in the retraction velocity of the outer droplet periphery. Hence, non-Newtonian elongation viscosity or contact line dissipation cannot explain the observed phenomenon. However, our study suggests that the suppression is instead induced by the early onset of a fingering instability in LM at $We \sim 57$.

As the droplet rebounds and tries to leave the surface, it stretches. Stretching depends on the remaining kinetic energy in the rebounding droplet and the surface adhesion. Droplet pinch-off through Rayleigh-Plateau (RP) instability is only possible beyond a critical stretching ratio (L_{max}/D_0), where L_{max} is the stretched length of the droplet during rebound (see, Inset Fig. 3(A)). As seen in Fig. 3(A), we identify the critical stretching ratio of $L_{max}/D_0 \sim 1.9$ in our experiments. As seen in Fig. 3(B), at the lowest D_{max} ($We < 20$), the stretched length (L_{max}) is approximately equal to the maximum spread diameter (D_{max}) in all cases. This behavior indicates an inviscid impact with negligible surface adhesion. However, we observe a continuous reduction in L_{max} for high mass loading LM at large impact velocities ($We > 57$). L_{max}/D_0 values reduce below the critical stretching ratio, and droplet pinch-off is suppressed. In contrast, L_{max} remains high for bare droplets. We attribute this reduction in L_{max} and the associated occurrence of the no-breakage island to an additional dissipation mechanism. This dissipation stems from an interfacial instability that leads to finger-like structures.

3.3. Rim instability

As the droplet reaches its maximum spread diameter, a rim of liquid is formed at the edge of the flattened droplet. At $We > 57$, an interfacial instability sets in during the spreading phase. As shown in Fig. 4(A) & (B) and Supplementary Video S4, this rim destabilizes as it expands, and perturbations can be seen in both bare droplets and LM. However, only in the LM case, these perturbations grow and form finger-like structures during the retraction phase. Finger formation is not observed for the bare droplet case at the same *We*. These fingers are different from viscous fingers. The capillary number ($Ca = \mu V/\gamma$) for the viscous fingering is more than unity ($Ca > 1$) [31,50,51]. However, in our case, the Capillary number is below 0.025, indicating this being an inertial-capillary fingering [50,51].

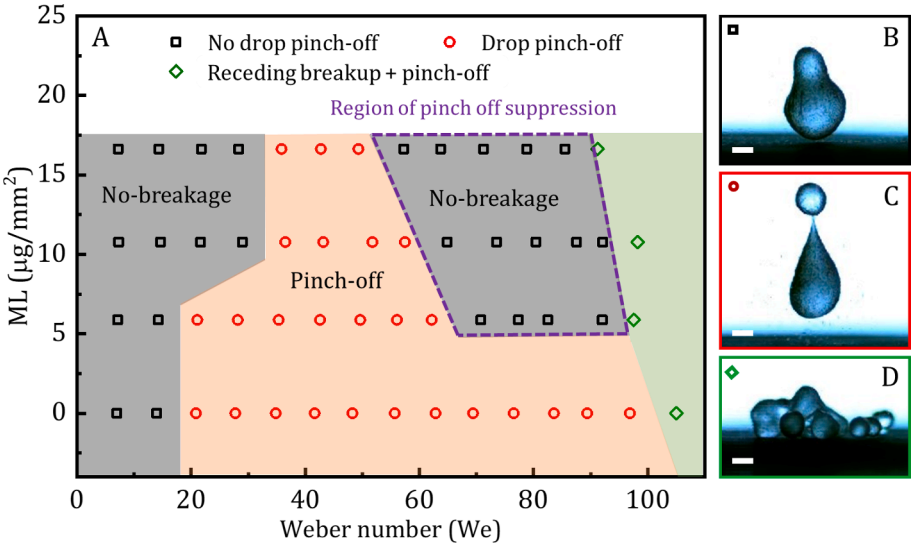

Fig. 2. (A) Droplet stability regime for different ML and impact *We*. Photographs of the different scenarios for ML = 5.87 μg/mm². (B) *No-pinch-off*: (black squares) represents the stable LM without any rupture or pinch-off. (C) *Pinch-off*: (red circles) droplet breaks from the top during rebound. (D) *Receding-breakup + Pinch-off*: (green diamonds) multiple droplets eject on the substrate during the retraction phase. Additionally, the process may involve simultaneous pinch-off events during the lift-off phase (Scale bar – 1 mm). (For interpretation of the references to colour in this figure legend, the reader is referred to the web version of this article.)

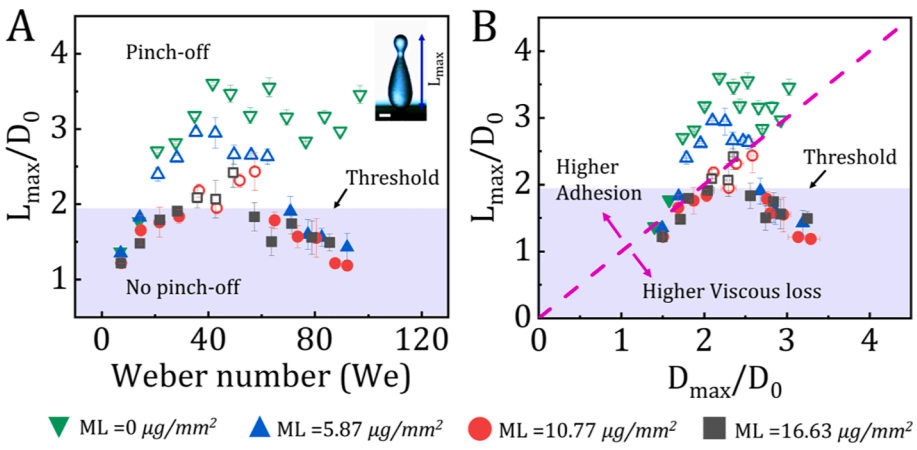

Fig. 3. (A) The normalized maximum extension is plotted against *We*. The colored region corresponds to $L_{max}/D_0 < 1.9$. Inset: representation of L_{max} during rebound. (Scale bar – 1 mm). (B) The normalized maximum extension is plotted against the normalized maximum diameter. Here, the dashed line corresponds to $L_{max} \cong D_{max}$. The data above the line represents higher adhesion energy, and the data below represents a higher viscous loss. The filled symbols represent the no pinch-off zone, while the open symbols represent the pinch-off regime.

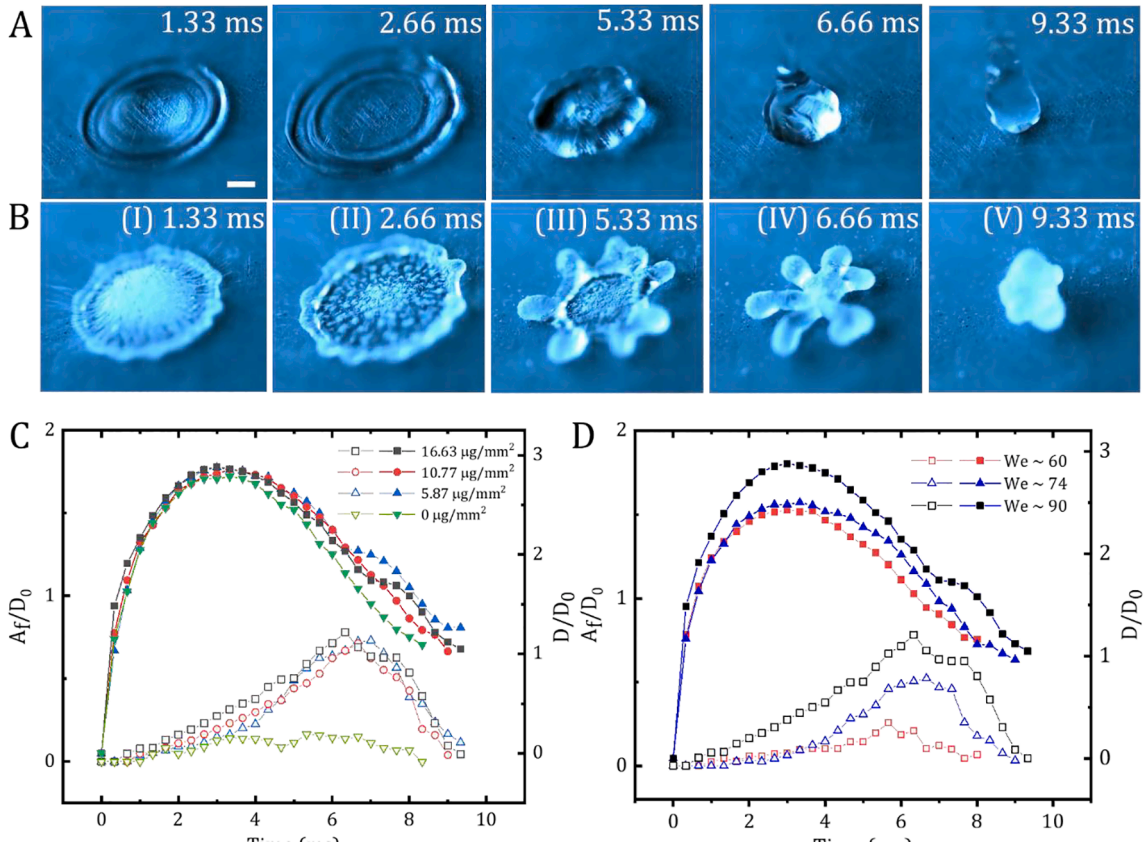

Fig. 4. (A) Sequential snapshots of a water droplet impacting the superhydrophobic surface for *We* ~ 77. (B) LM impact on the superhydrophobic surface at *We* ~ 77. Initial finger formation can be seen at the maximum spread. Scale = 1 mm. (C) Temporal evolution of normalized finger length (A_f/D_0) and diameter (D/D_0) for various ML at *We* ~ 90. The filled symbols represent the normalized diameter evolution (D/D_0), and the open symbols represent the normalized finger length (A_f/D_0). Here, A_f is the amplitude of the fingers. (D) Temporal evolution of normalized finger length and diameter for ML of 16.63 μg/mm^2 at different *We*.

Fig. 4(C) represents the temporal evolution of normalized finger length and spread diameter for *We* ~ 90. The evolution of diameter is nearly the same for all cases. While finger growth is seen for all LM's, the finger length remains negligible in the bare droplet case. Additionally, the growth of the perturbation is not limited to the spreading phase only. The perturbations grow faster after the droplet reaches its maximum spread state (~2.66 ms). Compared to bare droplets, perturbation at maximum spread is higher in LM as seen in Fig. 4(C). The finger growth is driven by the rapid retraction of the inner interface (D_{in}) between the fingers while the tips remain nearly stationary (Supplementary Fig. S2). For a particular LM, an increase in *We* results in increased spread diameter and finger length, as seen in Fig. 4(D).

The formation of fingers for a bare droplet is observed at a much higher Weber number (~110). However, these fingers are unstable, and they dissociate on the surface due to receding breakup. Supplementary Fig. S3(A) represents the variation in normalized finger length (A_f/D_0) at the maximum spread. At *We* below 110, the LM has a much higher amplitude compared to the bare droplet. However, above *We* ~ 110, a similar trend is observed. Maximum finger length also follows the same trend, and LM shows large finger growth even at lower *We* (Supplementary Fig. S3(B)).

3.3.1. Role of the initial perturbation

The growth of an unstable mode is represented by $A_f = A_o exp(\beta t)$, where A_o is the initial perturbation, β is the mode-specific growth rate, and t is the growth time [52]. We postulate that early finger formation in LM is because of the higher initial perturbations due to the trapped particles. During initial contact, particles get trapped between the spreading liquid and the superhydrophobic surface (Fig. 5(A)). The trapped particles render the bottom surface inhomogeneous. The contact line experiences wetting discontinuity at the edge of the trapped particle islands. This discontinuity is the reason for the higher initial perturbation.

A separate experiment was performed to verify the role of trapped particles. A small number of particles are pre-dispersed on the superhydrophobic surface. It is observed that fingering instability is triggered even for bare droplets at lower impact energies ($We \sim 72$), further confirming the role of initial perturbation (Fig. 5(B) & (C) and Supplementary Video S5). Similar behaviour is observed for bare droplet with a small island of particles attached at the bottom interface (Supplementary Fig. S3(C) and Supplementary Video S6). These observations confirm the predominant role of trapped particles in triggering finger growth at lower *We*.

3.3.2. Role of particle accumulation at the rim

Particle accumulation and distribution at the rim may also plays a role in the early onset finger formation. During the spreading phase, the fluid flows from the center toward the rim (see Supplementary Video S4). This causes an accumulation of the particles at the rim due to fluid drag [53]. Subsequently, as shown in Fig. 5(D), the initial perturbation

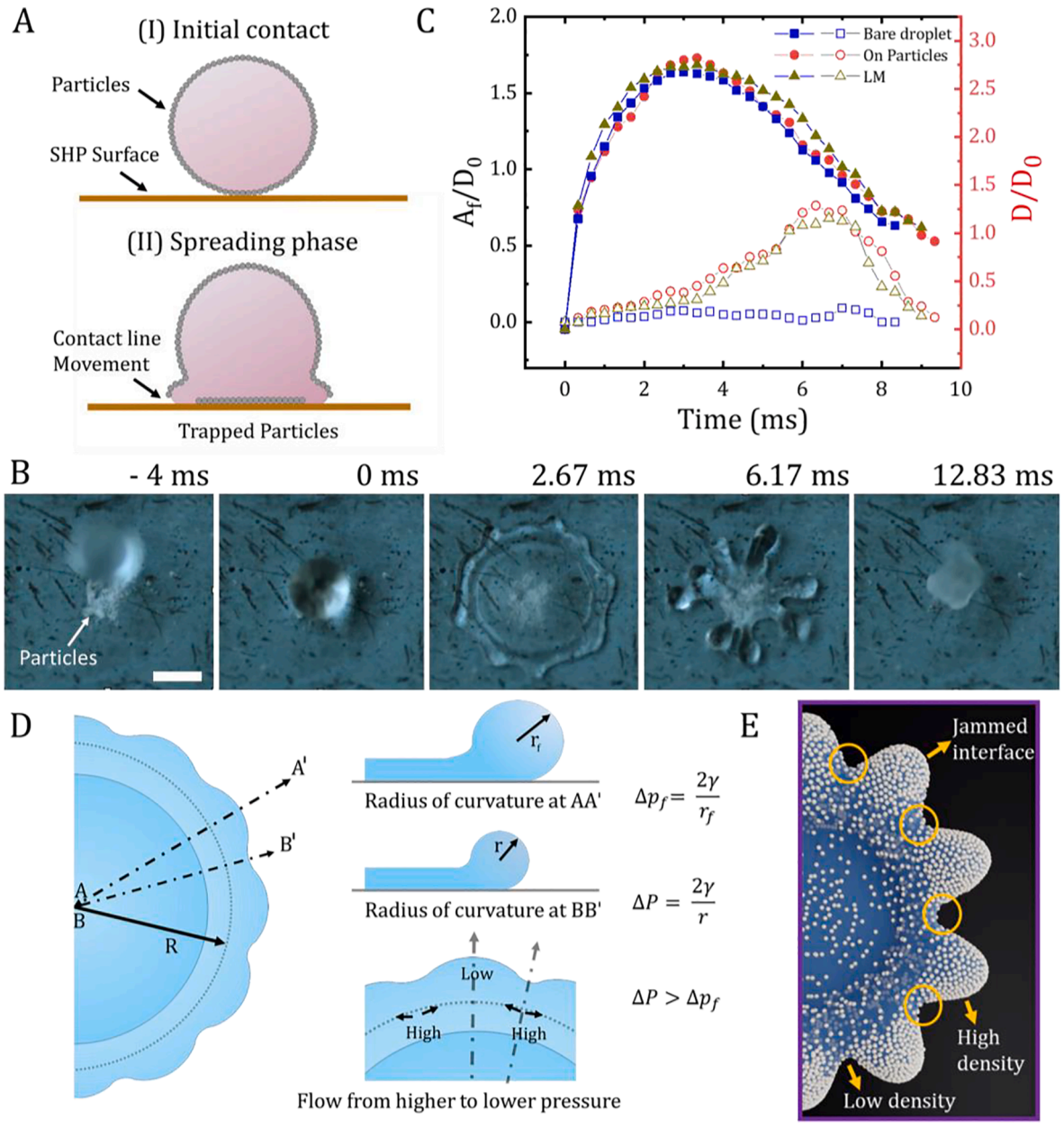

Fig. 5. (A) (I) Initial contact of LM with the superhydrophobic surface (II) Movement of contact line during a spreading phase where particles get trapped at the impact position. (B) Bare droplet impact over the surface with PTFE particles at $We \sim 72$ shows a similar finger formation, further confirming the role of initial perturbation and particles. Scale = 2 mm. (C) Temporal evolution of normalized finger length and diameter for bare droplet impacting on particle bed over a substrate at $We \sim 77$. The filled symbols represent the normalized diameter evolution (D/D_0), and the open symbols represent the normalized finger length (A_f/D_0). (D) Schematic representation of the growth of fingers due to Laplace pressure gradient. (E) The localized particle density change during the spreading of LM.

in the rim leads to the generation of a Laplace pressure gradient which drives the liquid and the particles toward the perturbation tip. As reported before, this is a manifestation of the Rayleigh-Plateau instability in toroidal geometry [13,54]. While the tangential flow promotes the growth of the perturbations, radial flow drives the fluid towards the center.

As seen in Fig. 4(A), the radial flow overshadows the tangential flow and suppresses perturbations growth for the bare droplet. However, in the case of LM, particles accumulate at the perturbation tip due to the tangential flow. As shown in Fig. 5(E), this accumulation results in particle jamming at the fingertips. Jamming hinders the retraction of the fingers (see Supplementary Section 1.3) and hence prevents the surface tension from stabilizing the rim shape. The dependence of the instability onset *We* on LM mass loading can be attributed to the accumulation and distribution of the particles at the rim (Fig. 2(A)).

3.4. Rim Bond number

In previous literature, the generation of fingers has been attributed to Rayleigh-plateau (RP) and Rayleigh-Taylor (RT) [13,14,27]. Previous work [14] has analyzed the stability of an inviscid cylindrical rim subjected to acceleration. The dispersion relation for the coupled effect is given in terms of nondimensionalized wavenumber (κ) and rim Bond number (Bo) as [14]

$$\omega^2 = 0.5\left\{ -\chi(\kappa) + \sqrt{\chi(\kappa)^2 - 4\psi(\kappa)} \right\}$$

$$\chi(\kappa) = \frac{\kappa I_1(\kappa)}{I_0(\kappa)}\left(\kappa^2 - 1\right) + \frac{\kappa I_2(\kappa)}{I_1(\kappa)}\kappa^2$$

$$\psi(\kappa) = \frac{\kappa^2 I_2(\kappa)}{2I_0(\kappa)}\left[2\left(\kappa^2 - 1\right)\kappa^2 - \left(\frac{Bo}{4}\right)^2\right] \quad (1)$$

Where ω is the growth rate non-dimensionalized by rim capillary time ($\tau_r \sim \sqrt{\rho b^3/8\gamma}$). κ is perturbation wavenumber non-dimensionalized by rim radius ($b/2$) (see Fig. 6(A)). $I_n(\kappa)$ is the modified Bessel function of the first kind of order n. Bo is the rim Bond number given by $\rho a b^2/\gamma$, where a is the rim deceleration. Dispersion curves (Eq. (1)) for different rim Bond numbers are plotted in Supplementary Fig. S4. For the range of Bo observed in our experiments, the curves remain close to that of the pure RP instability.

Fig. 6(A) plots the normalized finger length (A_f) at maximum spread with rim Bond number. Here, deceleration is approximated as $a \cong D_{max,in}/t_m^2$, where $D_{max,in}$ is the inner rim diameter at the maximum spread, as shown in Fig. 6(A) inset. From the collapse of the data, we can conclude that finger formation is well explained with the rim Bond number. As rim width (b) decreases with an increase in *We* (Supplementary Fig. S5), higher impact velocities lead to lower Bo. Hence, the amplitude (A_f) is observed to increase with the decrease in the rim Bond number. Supplementary Fig. S6 plots normalized A_{max} with the rim Bond number. Below a critical Bo (~4), where the initial finger length is high ($A_f/D_0 > 0.07$), the fingers grow during the retraction phase. At higher Bo where $A_f/D_0 < 0.07$, the finger growth is restricted.

Fig. 6(B) plots the maximum finger length attained during the retraction phase as a function of the finger length at D_{max}. We observe that the maximum finger length (A_{max}) grows significantly only beyond a critical initial finger length (A_f). Finger length is determined by the growth rate of the fastest growing unstable mode. Supplementary Fig. S7 shows the theoretical growth rate for the fastest growing mode with Bo. Mode growth time, given by $t_g = \tau_r/\omega$ is plotted in Supplementary Fig. S8. τ_r is evaluated from the experimentally measured rim width (b), and ω is extracted from the theoretical curve shown in Supplementary Fig. S7. Growth time for the fastest mode increases with Bo. This explains the larger amplitude at smaller Bo. This also explains significant growth of finger length only after a critical initial perturbation (Fig. 6 (B)). Only for cases where the mode growth time (t_g) is significantly smaller than the spread time (t_m), the perturbation has sufficient time to grow.

In Supplementary Video S1, we observe that the initial ejection during impact of particle-coated droplets (LM) at $We = 35$, which occurs predominantly from loosely bound particles. The multilayered particle coating on high mass loading LM contains some particles that are not tightly adhered to the liquid surface, resulting in their ejection upon impact. In contrast, Supplementary Video S4 (and Fig. 4) show that particle ejection is not observed for bare water.

3.5. Effect of viscous loss

During droplet rebound, the finger formation accounts for additional energy dissipation. To estimate additional losses due to finger collapse,

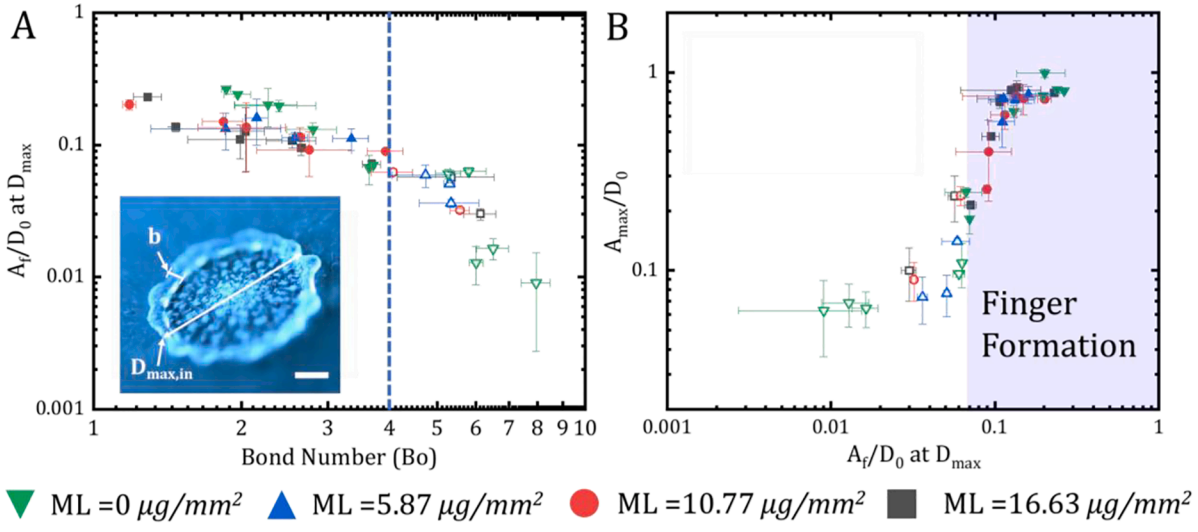

Fig. 6. (A) Variation of normalized finger length (A_f/D_0) at maximum spread diameter for different rim Bond numbers. The dotted line represents the critical Bond number. Inset: the LM at maximum spread where the rim width is given by b and inner rim diameter is given by $D_{max,in}$. (B) The maximum amplitude of the fingers is plotted against the amplitude at the maximum spread. Above critical value of $A_f/D_0 \sim 0.07$, the finger formation is predominant. Additionally, all data collapse into one single curve, representing amplitude at maximum spread giving rise to elongated fingers at lower *We* in LM. The filled symbols represent the finger formation during retraction, while the open symbols represent the no fingers during the retraction phase.

the restitution coefficient $\varepsilon = (KE_f/KE_i)^{0.5}$ and normalized total energy is plotted in Fig. 7(A) & (B), respectively. KE_f and KE_i are final and initial kinetic energy, respectively. The initial state is when LM touches the superhydrophobic surface, which corresponds to the 0 ms time instant. While the final state of the LM is when LM achieves maximum height after the rebound. The time instant of the final state varies from 33 ms to 55 ms. The energy is calculated by tracking the center of mass of the droplet. The detailed calculation of energies given in Supplementary Section 1.4. It is evident from Fig. 7(A) that the occurrence of the no-breakage island coincides with a faster reduction in the restitution coefficient with *We*. Up to $\varepsilon \sim 0.31$, the LM follows the scaling of $\sim We^{-0.27}$ for the restitution coefficient. This is approximately the same scaling as observed for a bare droplet ($\sim We^{-0.25}$) [55]. However, after that, the restitution coefficient follows a different scaling of $\varepsilon \sim We^{-1.36}$. This proves the existence of additional energy dissipation due to the retraction and collapse of fingers in LM. Whereas the bare droplet continues to follow $\varepsilon \sim We^{-0.25}$ even at higher Weber numbers (Inset, Fig. 7(A)). Similarly, the final energy drops significantly in the case of LM after finger formation (Fig. 7(B)).

Normalized energy loss in the pinch-off suppression regime is plotted in Fig. 8(A). We hypothesize that the additional energy loss during the collapse of such fingers depends on the viscous flow in the fingers. The energy loss during retraction mainly depends on the shear stress in the elongated fingers, total numbers (N_f) and the length of the fingers (A_f). The shear stress in the fingers can be estimated as $\mu V_{ret}/D_f$, where μ, V_{ret}, r_f are the liquid viscosity, retraction velocity, and finger diameter, respectively. Thus, the energy loss ($KE_i - KE_f$) should scale with $\mu V_{ret} N_f A_f^2$. The velocity of retraction depends upon the Taylor-Culick relation: $V_{ret} \sim (\gamma/\rho D_f)^{0.5} \sim VWe^{-0.25}$, where V is the velocity of impact and $D_f \sim D_0^3/D_{max}^2$ derived from volume conservation [56]. From the previous scaling arguments, $N_f \sim We^{3/8}$ and $A_f \sim D_{max} \sim D_0 We^{0.25}$ because of the major growth of fingers during the retraction phase (refer Supplementary Figure S9). The initial kinetic energy (KE_i) scales as $\rho V^2 D_0^3$. Thus, the normalized loss should scale with

$$\frac{KE_i - KE_f}{KE_i} \sim \frac{We^{5/8}}{Re} \tag{2}$$

where *Re* is the Reynolds number. Fig. 8(A) shows scaling according to Eq. (2), which agrees very well with the experiments.

Despite forming prominent fingers ($A_{max} > 1$ mm), we do not observe its breakage into smaller droplets. As $A_f \sim D_{max}$, at lower *We*, the resultant finger length is insufficient to destabilize and break into droplets. Finger breakage due to RP instability in jets [57] is possible when the $A_{max}/D_f > \pi$. Fig. 8(B) represents the ratio of maximum finger length (A_{max}) and finger diameter (D_f). The critical ratio for the breakup of fingers was determined by measuring the diameter and length of the finger just before it breaks (Inset Fig. 8(B)). We found the critical ratio of $A_{max}/D_f \sim 3.8$ is required for the breakup of the fingers. Despite prominent fingers in $57 < We < 92$ regions, the A_{max}/D_f ratio for LM remains lower than the critical limit. Thus, fingers remain stable without dissociation. Various droplet breakage phenomenon with relevant mechanisms and dominant instability is summarized in Supplementary Table S1.

4. Conclusion

"Hydrophobic particle coating over droplets remarkably affects the stability of impacting droplets. Previous works on particle-coated droplet impact were limited to studying spreading dynamics and related applications [20,24,25,58,59]. The present paper reports an early onset of a unique interfacial instability region in the impact of particle-coated droplets at *We* (57 to 92). In contrast, this instability is observed at twice the impact energy for bare droplets. The instability suppresses the pinch-off in LM, which is inevitable in the case of the bare droplet. This leads to the observation of an anomalous "no pinch-off" island (the stability region emerges in-between unstable regions). During impact, the maximum spreading diameter and maximum spreading time remain nearly the same for both LM and bare droplet. These observations imply that the liquid surface tension governs the spreading dynamics. Pinch-off suppression in LM is attributed to the reduced extension of the LM during rebound, which suppresses the necking by RP instability. The reduced extension further indicates higher losses in LM in the "no pinch-off" regime. The temporal evolution of the spreading radius is also similar for bare droplet and LM's of different particle loadings. This indicates the absence of increased contact line dissipation or non-Newtonian behaviour [48,49]. Contrary to bare droplets, the early formation of the fingering instability in LM was found to be the reason behind the anomalous no-pinch off island. The formation of the fingers is attributed to the trapped particles during the initial phase of impact, which induces roughness-based wettability contrast. Additionally, a change in particle density over a contact line plays a role in the formation and elongation of the fingers. Further, it has been established that finger formation in LM is characterized by the rim Bond number,

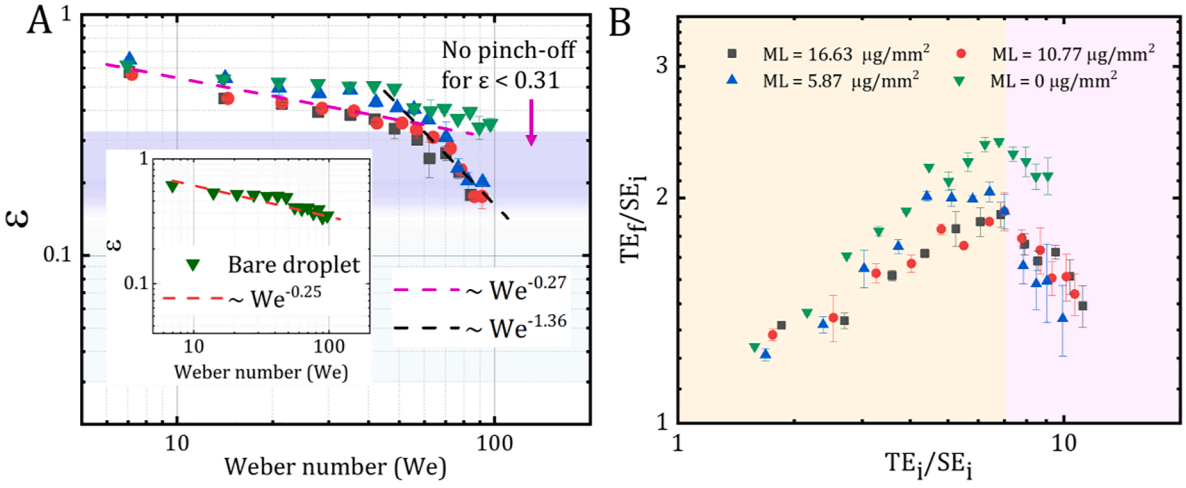

Fig. 7. (A) Restitution coefficient of the main droplet. Legend is shown in part (B). The colored region indicates the value of ε below 0.31. Restitution follows the scaling of slope −0.27 up to $\varepsilon = 0.31$. Consequently, a faster decay in restitution (with a −1.36 slope) is observed (colored region). In contrast, the bare droplet follows the standard scaling of −0.25 up to receding breakup (Inset). (B) Final total energy (TE_f) normalized by initial surface energy (SE_i) is plotted against normalized total initial energy (TE_i/SE_i). The boundary of the colored regions represents the starting of energy loss.

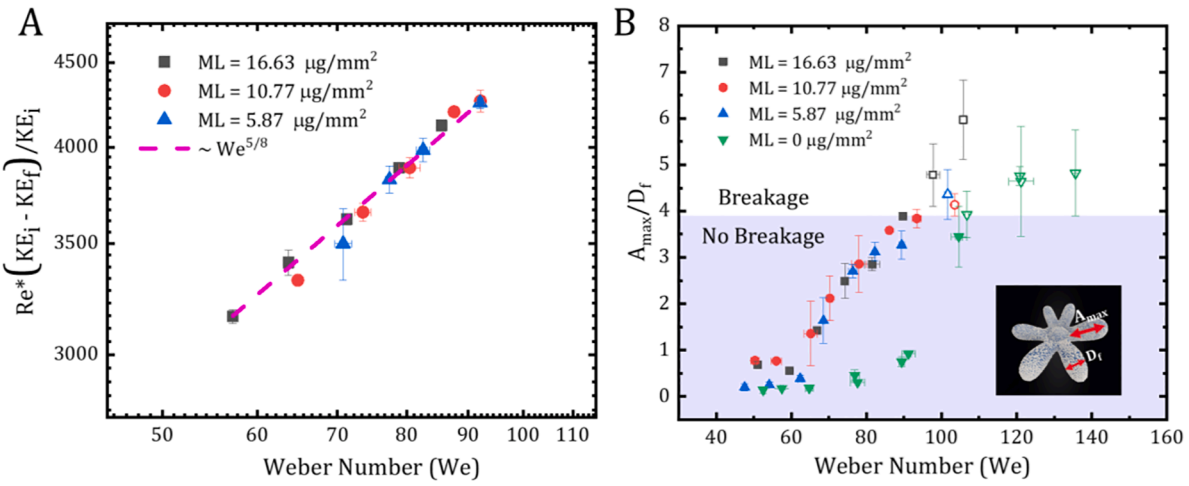

Fig. 8. (A) Normalized energy loss plotted against Weber number. The scaling of slope 5/8 matches very well with experimental results. (B) The ratio of maximum finger length (A_{max}) to finger diameter (D_f) is plotted against the *We*. The colored region indicates below critical $A_{max}/D_f \sim 3.8$, where no breakage of fingers is present. Inset: Schematic representation of maximum finger length (A_{max}) to finger diameter (D_f). The filled symbols represent the breakage of the fingers, while the open symbols represent the no breakage regime.

which confirms the combined role of RP and RT instability in destabilizing the rim and forming fingers [14]. Finger growth is observed at the lower rim Bond number due to a shorter growth time for the fastest mode. Significant finger formation is observed only when the mode growth time is sufficiently shorter than the spread time. The formation of such elongated fingers accounts for additional viscous loss, which suppresses droplet pinch-off during rebound. The proposed scaling matches well with the experimental data. The RP instability sets a critical dimension for finger length beyond which the fingers break while they remain intact before reaching this limit. This leads to additional dissipation during retraction, effectively suppressing droplet pinch-off."

Declaration of Competing Interest

The authors declare that they have no known competing financial interests or personal relationships that could have appeared to influence the work reported in this paper.

Data availability

Data will be made available on request.

Acknowledgments

The authors would like to acknowledge the National Nanofabrication Centre and the Micro/Nano Characterization Facility at CeNSE, IISc, for the fabrication and characterization facility. The authors also acknowledge Arun Singh Baghel and Vaibhav Singh Rajput for their help in image analysis code. All the authors would like to thank the Department of Science and Technology and the Ministry of Education, Government of India for financial support. RL acknowledges Prime Minister's Research Fellowship for the financial support.

Appendix A. Supplementary material

Supplementary data to this article can be found online at https://doi.org/10.1016/j.jcis.2023.05.067.

References

[1] A.U. Siddique, M. Trimble, F. Zhao, M.M. Weislogel, H. Tan, Jet ejection following drop impact on micropillared hydrophilic substrates, Phys. Rev. Fluids. 5 (2020), 063606, https://doi.org/10.1103/PhysRevFluids.5.063606.

[2] D. Bartolo, C. Josserand, D. Bonn, Singular jets and bubbles in drop impact, Phys. Rev. Lett. 96 (2006), 124501, https://doi.org/10.1103/PhysRevLett.96.124501.

[3] X. Deng, C. Huang, S. Liu, C. Yang, P. Wu, J. He, W. Jiang, Urea melt marbles developed by enwrapping urea melt droplets with superhydrophobic particles: preparation, properties, and application in large urea granule production, Adv. Mater. Interfaces. 8 (2021) 2100253, https://doi.org/10.1002/ADMI.202100253.

[4] M. Damak, M.N. Hyder, K.K. Varanasi, Enhancing droplet deposition through in-situ precipitation, Nat. Commun. 2016 71. 7 (2016) 1–9. https://doi.org/10.1038/ncomms12560.

[5] S. Kim, H. Park, H.A. Gruszewski, D.G. Schmale, S. Jung, Vortex-induced dispersal of a plant pathogen by raindrop impact, Proc. Natl. Acad. Sci. 116 (11) (2019) 4917–4922.

[6] S. Nath, S.F. Ahmadi, H.A. Gruszewski, S. Budhiraja, C.E. Bisbano, S. Jung, D. G. Schmale, J.B. Boreyko, 'Sneezing' plants: pathogen transport via jumping-droplet condensation, J. R. Soc. Interface. 16 (155) (2019) 20190243.

[7] D. Roy, M. Sophia, A. Rasheed, P. Kabi, A.S. Roy, R. Shetty, S. Basu, Fluid dynamics of droplet generation from corneal tear film during non-contact tonometry in the context of pathogen transmission, Phys. Fluids. 33 (2021), 092109, https://doi.org/10.1063/5.0061956/5.0061956.MM.ORIGINAL.V1.AVI.

[8] A. Tripathy, G. Muralidharan, A. Pramanik, P. Sen, Single etch fabrication and characterization of robust nanoparticle tipped bi-level superhydrophobic surfaces, RSC Adv. 6 (2016) 81852–81861, https://doi.org/10.1039/c6ra16312b.

[9] Z. Liu, X. Pan, Q. Ma, H. Fang, Receding dynamics of droplet deposition on a smooth surface from a central jet to secondary droplet emission, Langmuir 36 (2020) 15082–15093, https://doi.org/10.1021/acs.langmuir.0c02643.

[10] L. Yang, Z. Li, T. Yang, Y. Chi, P. Zhang, Experimental study on droplet splash and receding breakup on a smooth surface at atmospheric pressure, Langmuir 37 (2021) 10838–10848, https://doi.org/10.1021/acs.langmuir.1c01797.

[11] A.L. Yarin, Drop impact dynamics: splashing, spreading, receding, bouncing…, Annu. Rev. Fluid Mech. 38 (1) (2006) 159–192.

[12] M. Reyssat, A. Pépin, F. Marty, Y. Chen, D. Quéré, Bouncing transitions on microtextured materials, EPL (Europhysics Lett. 74 (2) (2006) 306–312.

[13] X. Huang, K.-T. Wan, M.E. Taslim, Axisymmetric rim instability of water droplet impact on a super-hydrophobic surface, Phys. Fluids. 30 (9) (2018) 094101.

[14] Y. Wang, R. Dandekar, N. Bustos, S. Poulain, L. Bourouiba, Universal rim thickness in unsteady sheet fragmentation, Phys. Rev. Lett. 120 (2018), 204503, https://doi.org/10.1103/PHYSREVLETT.120.204503/FIGURES/4/MEDIUM.

[15] C. Clanet, C. Béguin, D. Richard, D. Quéré, Maximal deformation of an impacting drop, J. Fluid Mech. 517 (2004) 199–208, https://doi.org/10.1017/S0022112004000904.

[16] D. Khojasteh, M. Kazerooni, S. Salarian, R. Kamali, Droplet impact on superhydrophobic surfaces: A review of recent developments, J. Ind. Eng. Chem. 42 (2016) 1–14, https://doi.org/10.1016/j.jiec.2016.07.027.

[17] C. Planchette, E. Lorenceau, A.L. Biance, Surface wave on a particle raft, Soft Matter 8 (2012) 2444–2451, https://doi.org/10.1039/c2sm06859a.

[18] R. Lathia, P. Sen, Sol–gel-derived nanoparticles coated liquid entities: liquid marbles, liquid plasticine, and flat interface, J. Micromech. Microeng. 33 (2) (2023) 024002.

[19] T. Supakar, A. Kumar, J.O. Marston, Impact dynamics of particle-coated droplets, Phys. Rev. E. 95 (2017) 1–10, https://doi.org/10.1103/PhysRevE.95.013106.

[20] C. Planchette, A.L. Biance, E. Lorenceau, Transition of liquid marble impacts onto solid surfaces, EPL 97 (1) (2012) 14003.

[21] C. Planchette, A.-L. Biance, O. Pitois, E. Lorenceau, Coalescence of armored interface under impact, Phys. Fluids. 25 (4) (2013) 042104.

[22] J. Jin, C.H. Ooi, D.V. Dao, N.T. Nguyen, Liquid marble coalescence: Via vertical collision, Soft Matter 14 (2018) 4160–4168, https://doi.org/10.1039/c8sm00121a.
[23] Y. Feng, L. Wang, J. Xu, G. Liu, Effect of particle size on the stripping dynamics during impact of liquid marbles onto a liquid film, Soft Matter 18 (2022) 5230–5238, https://doi.org/10.1039/D2SM00506A.
[24] B.S. Lekshmi, A.S. Yadav, P. Ranganathan, S.N. Varanakkottu, Simple and continuous fabrication of janus liquid marbles with tunable particle coverage based on controlled droplet impact, Langmuir 36 (2020) 15396–15402, https://doi.org/10.1021/acs.langmuir.0c02988.
[25] B.S. Lekshmi, S.N. Varanakkottu, Droplet-impact driven formation of ultralow volume liquid marbles with enhanced mechanical stability and sensing ability, Langmuir 38 (2022) 11743–11752, https://doi.org/10.1021/ACS.LANGMUIR.2C01880.
[26] R. Gupta, V. Vaikuntanathan, D. Sivakumar, Superhydrophobic qualities of an aluminum surface coated with hydrophobic solution NeverWet, Colloids Surfaces A Physicochem. Eng. Asp. 500 (2016) 45–53, https://doi.org/10.1016/J.COLSURFA.2016.04.017.
[27] S. Shakeri, S. Chandra, Splashing of molten tin droplets on a rough steel surface, Int. J. Heat Mass Transf. 45 (2002) 4561–4575, https://doi.org/10.1016/S0017-9310(02)00170-9.
[28] H. Marmanis, S.T. Thoroddsen, Scaling of the fingering pattern of an impacting drop, Phys. Fluids. 8 (1996) 1344–1346, https://doi.org/10.1063/1.868941.
[29] A. Hooshanginejad, B.C. Druecke, S. Lee, Stability analysis of a particle band on the fluid–fluid interface, J. Fluid Mech. 869 (2019) 2, https://doi.org/10.1017/JFM.2019.239.
[30] M. Bussmann, S. Chandra, J. Mostaghimi, Modeling the splash of a droplet impacting a solid surface, Phys. Fluids. 12 (12) (2000) 3121–3132.
[31] M. Ferer, C. Ji, G.S. Bromhal, J. Cook, G. Ahmadi, D.H. Smith, Crossover from capillary fingering to viscous fingering for immiscible unstable flow: Experiment and modeling, Phys. Rev. E - Stat. Physics, Plasmas, Fluids, Relat. Interdiscip. Top. 70 (2004) 7, https://doi.org/10.1103/PHYSREVE.70.016303/FIGURES/9/MEDIUM.
[32] F. Geyer, M. D'Acunzi, A. Sharifi-Aghili, A. Saal, N. Gao, A. Kaltbeitzel, T.-F.-F. Sloot, R. Berger, H.-J.-J. Butt, D. Vollmer, When and how self-cleaning of superhydrophobic surfaces works, Sci. Adv. 6 (2020) eaaw9727, https://doi.org/10.1126/SCIADV.AAW9727/SUPPL_FILE/AAW9727_SM.PDF.
[33] X. Yan, B. Ji, L. Feng, X. Wang, D. Yang, K.F. Rabbi, Q. Peng, M.J. Hoque, P. Jin, E. Bello, S. Sett, M. Alleyne, D.M. Cropek, N. Miljkovic, Particulate-Droplet Coalescence and Self-Transport on Superhydrophobic Surfaces, ACS Nano 16 (2022) 12910–12921, https://doi.org/10.1021/ACSNANO.2C05267.
[34] A. Sayyah, M.N. Horenstein, M.K. Mazumder, Energy yield loss caused by dust deposition on photovoltaic panels, Sol. Energy. 107 (2014) 576–604, https://doi.org/10.1016/J.SOLENER.2014.05.030.
[35] M. Ghanbari, G. Rezazadeh, A liquid-state high sensitive accelerometer based on a micro-scale liquid marble, Microsyst. Technol. 26 (2020) 617–623, https://doi.org/10.1007/s00542-019-04528-7.
[36] B. Wang, K.F. Chan, F. Ji, Q. Wang, P.W.Y. Chiu, Z. Guo, L. Zhang, On-Demand Coalescence and Splitting of Liquid Marbles and Their Bioapplications, Adv. Sci. 6 (2019) 1802033, https://doi.org/10.1002/advs.201802033.
[37] P.K. Roy, B.P. Binks, S. Fujii, S. Shoval, E. Bormashenko, S. Fujii, S. Shoval, E. Bormashenko, Composite Liquid Marbles as a Macroscopic Model System Representing Shedding of Enveloped Viruses, J. Phys. Chem. Lett. 11 (2020) 4279–4285, https://doi.org/10.1021/acs.jpclett.0c01230.
[38] E. Jambon-Puillet, T.J. Jones, P.-T. Brun, Deformation and bursting of elastic capsules impacting a rigid wall, Deformation and bursting of elastic capsules impacting a rigid wall 16 (5) (2020) 585–589.
[39] C.H. Ooi, R. Vadivelu, J. Jin, K.R. Sreejith, P. Singha, N.-K.-N.-T. Nguyen, N.-K.-N.-T. Nguyen, Liquid marble-based digital microfluidics – fundamentals and applications, Lab Chip. 21 (2021) 1199–1216, https://doi.org/10.1039/D0LC01290D.
[40] G. McHale, M.I. Newton, Liquid marbles: Principles and applications, Soft Matter 7 (2011) 5473–5481, https://doi.org/10.1039/c1sm05066d.
[41] M. Tenjimbayashi, S. Samitsu, Y. Watanabe, Y. Nakamura, M. Naito, Liquid Marble Patchwork on Super-Repellent Surface, Adv. Funct. Mater. (2021) 2010957. https://doi.org/10.1002/adfm.202010957.
[42] A. Kumar, A. Tripathy, C.D. Modak, P. Sen, Designing assembly of meshes having diverse wettability for reducing liquid ejection at terminal velocity droplet impact, J. Microelectromechanical Syst. 27 (2018) 866–873, https://doi.org/10.1109/JMEMS.2018.2850903.
[43] R. Lathia, B.S. Reddy, C. Dey Modak, S. Nagpal, P. Sen, Temperature-Responsive Microcapsules Manufactured by Promoting Controlled Cloaking with the Help of Micro/Nanoparticles, 2023 IEEE 36th Int. Conf. Micro Electro Mech. Syst. (2023) 1088–1090. https://doi.org/10.1109/MEMS49605.2023.10052506.
[44] R. Wang, X. Li, On the effective surface tension of powder-derived liquid marbles, Powder Technol. 367 (2020) 608–615, https://doi.org/10.1016/j.powtec.2020.04.028.
[45] H. Hoffman, R. Sijs, T. De Goede, D. Bonn, Controlling droplet deposition with surfactants, Phys. Rev. Fluids. 6 (2021), 033601, https://doi.org/10.1103/PHYSREVFLUIDS.6.033601/FIGURES/7/MEDIUM.
[46] M. Aytouna, D. Bartolo, G. Wegdam, D. Bonn, S. Rafaï, Impact dynamics of surfactant laden drops: Dynamic surface tension effects, Exp. Fluids. 48 (2010) 49–57, https://doi.org/10.1007/S00348-009-0703-9/FIGURES/8.
[47] S. Lin, D. Wang, L. Zhang, Y. Jin, Z. Li, E. Bonaccurso, Z. You, X. Deng, L. Chen, Macrodrop-Impact-Mediated Fluid Microdispensing, Adv. Sci. 8 (2021) 2101331, https://doi.org/10.1002/ADVS.202101331.
[48] V. Bergeron, D. Bonn, J.Y. Martin, L. Vovelle, Controlling droplet deposition with polymer additives, Nature 405 (6788) (2000) 772–775.
[49] M.I. Smith, V. Bertola, Effect of polymer additives on the wetting of impacting droplets, Phys. Rev. Lett. 104 (2010) 1–4, https://doi.org/10.1103/PhysRevLett.104.154502.
[50] P. Mora, G. Morra, D.A. Yuen, R. Juanes, Influence of Wetting on Viscous Fingering Via 2D Lattice Boltzmann Simulations, Transp. Porous Media. 138 (2021) 511–538, https://doi.org/10.1007/S11242-021-01629-8/FIGURES/18.
[51] Y.F. Chen, S. Fang, D.S. Wu, R. Hu, Visualizing and quantifying the crossover from capillary fingering to viscous fingering in a rough fracture, Water Resour. Res. 53 (2017) 7756–7772, https://doi.org/10.1002/2017WR021051.
[52] Y. Wang, L. Bourouiba, Growth and breakup of ligaments in unsteady fragmentation, J. Fluid Mech. 910 (2021) A39, https://doi.org/10.1017/JFM.2020.698.
[53] Y. Zhao, J.S. Marshall, Spin coating of a colloidal suspension, Phys. Fluids. 20 (4) (2008) 043302.
[54] K. Fukudome, Y. Muto, K. Yamamoto, H. Mamori, M. Yamamoto, Numerical simulation of the solidification phenomena of single molten droplets impinging on non-isothermal flat plate using explicit moving particle simulation method, Int. J. Heat Mass Transf. 180 (2021), 121810, https://doi.org/10.1016/J.IJHEATMASSTRANSFER.2021.121810.
[55] D.G.K. Aboud, A.-M. Kietzig, On the oblique impact dynamics of drops on superhydrophobic surfaces. part II: Restitution coefficient and contact time, Langmuir 34 (2018) 9889–9896, https://doi.org/10.1021/ACS.LANGMUIR.8B01233.
[56] Z. Hu, F. Chu, X. Wu, Double-peak characteristic of droplet impact force on superhydrophobic surfaces, Extrem. Mech. Lett. 52 (2022) 101665.
[57] A.L. Yarin, I.V. Roisman, C. Tropea, Collision phenomena in liquids and solids, Collis, Phenom. Liq. Solids. (2017) 1–614, https://doi.org/10.1017/9781316556580.
[58] M. Tenjimbayashi, S. Fujii, M. Tenjimbayashi, S. Fujii, How liquid marbles break down: direct evidence for two breakage scenarios, Small 17 (2021) 2102438, https://doi.org/10.1002/SMLL.202102438.
[59] T. Supakar, M. Moradiafrapoli, G.F. Christopher, J.O. Marston, Spreading, encapsulation and transition to arrested shapes during drop impact onto hydrophobic powders, J. Colloid Interface Sci. 468 (2016) 10–20, https://doi.org/10.1016/j.jcis.2016.01.028.